





Expanding the memory effect in scattering imaging by manipulating photon distributionsZhengjia Zhang , Zhengjun Liu ,* and Shutian Liu †*School of Physics, Harbin Institute of Technology, Harbin 150001, China* (Received 22 February 2022; revised 5 August 2022; accepted 21 September 2022; published 11 October 2022)

Speckle correlation techniques based on the memory effect can recover objects from multiple scattered light without the information of the scattering media. The existing methods, however, are limited by the inherent angular width of the memory effect, and the retrieval algorithms frequently converge to erroneous solutions. In this paper, we propose an autoshrinking algorithm to expand the field of view in scattering imaging. We also develop a pretreatment iteration scheme to achieve high accuracy reconstruction. The autoshrinking method improves the quality of the energy spectrum by adaptively shrinking the speckle autocorrelation to its expanded central peak region and enhancing the ratio of the ballistic photons to the scattered photons. In the pretreatment iteration, the Brenner gradient function of a short testing iteration is employed to select the initial random Fourier phase to ensure the iteration can quickly and accurately converge. Experiments and simulations successfully confirm the effectiveness of our method.

DOI: [10.1103/PhysRevA.106.043508](https://doi.org/10.1103/PhysRevA.106.043508)**I. INTRODUCTION**

Imaging through scattering media is a tough task and yet a powerful tool in various applications [1–7], such as seeing aircrafts and vehicles through the foggy atmosphere [8–11], detecting cells through biological turbid media [12–14], and underwater optical communications [15–17]. The current scattering imaging techniques include acousto-optic imaging [18], transmission matrix measurements [19–21], phase conjugation imaging [22], point spread function [23–25], optical time of flight [26], and super-resolution scattering imaging [27–29]. The above techniques need to measure or control the wavefronts of the light field on two sides of the scattering media. These measurements are not available in some applications, for instance, in the living organisms for biomedical imaging. Hence, it is significant to develop the scattering imaging for reconstructing the object behind the multiple-scattering regime without disturbing the scattering media. Such a difficulty of scattering imaging without knowing the information of the scatterer can be avoided by considering the correlation in speckle intensity, or so-called memory effect. It indicates that beyond the multiple-scattering process, there still exist ballistic photons that can transmit directly through the scatterer without scattering. The ballistic photons can preserve the information of the incident wave or the objects [30–33]. These speckle correlation techniques based on the memory effect can perform noninvasive imaging of the object hidden behind the scatterer [14,30,34–37].

The single-shot imaging via speckle correlations suffered from a limited field of view (FOV) and a low success rate of reconstruction [30,34]. In particular, the FOV is usually much narrower than the width limited by the memory effect.

Various approaches were proposed to increase the maximum angular width of the memory effect include low-pass filtering [38], scaling-vector-based detection [39], and effective energy ratio [40]. However, these imaging methods have not exceeded the theoretical predicted width of the memory effect for the object in which all parts are connected. It is difficult to expand the memory effect for such integrated object because the ballistic photons within the scattering field should “remember” the information of the entire object. It is relatively easier to recover several isolated objects with each object having its own memory effect. Expanding the width of the memory effect depends extensively on the recovery of the distribution of ballistic photons. Indeed, the number of ballistic photons decreases rapidly with the thickness of the scattering layers increasing. Obviously, it is still necessary to find approaches to collect more ballistic photons and reduce the multiple scattered ones. In this process of manipulating photon distributions, the scattered photons cannot be eliminated completely. Therefore, the successful retrieval of the objects from noise-contaminated information is another tough task. Several reconstruction approaches have been proposed to improve the accurate convergence of phase retrieval for prior-free and real-time processing [13,40,41]. More effective algorithms to speed up the retrieval with high accuracy are still in demand.

In this paper, we present a strategy that can expand the FOV with high accuracy for the speckle correlation imaging. We manipulate the distribution of the ballistic photons by a small aperture in the spatial domain and propose an autoshrinking (AS) algorithm to select more intensities of the ballistic photons and suppress noises caused by the scattered photons. The small aperture filter is a spatial-angular approach to grossly reduce background noise intensity from the multiple-scattered light. The autoshrinking algorithm expands the range of high-fidelity imaging by retaining the ballistic photons and eliminate the noises in the entire

*Corresponding author: zjliu@hit.edu.cn†Corresponding author: stliu@hit.edu.cn

autocorrelation of the speckle pattern. By autoshrinking, we mean that we can adaptively choose and expand the central part of the autocorrelation peak of the speckle intensity pattern. In addition, to enhance the convergence and the accuracy of the calculation, we propose a pretreatment iteration algorithm to speed up the reconstruction. It implies that compared with the previous works [13,40,41], a precise convergence, even for a complex structured object, can be achieved by employing the autoshrinking algorithm and the pretreatment iteration algorithm sequentially. In the pretreatment iteration, a no-reference perceptual quality assessment is utilized in an initialization pretreatment process, which determines the choice of the random initial Fourier phase and the necessity of the following iterations. We have experimentally and numerically demonstrated the effectiveness of our approach.

II. ALGORITHMS OF IMAGING PROCESS

Single-shot intensity correlation scattering imaging technique retrieves the intensity of the object solely depends on the speckle pattern after its information passing through a scattering medium. The information of the object correlates with the speckle pattern by their autocorrelation distributions, even though the speckle pattern itself is a random distribution. The correlation between two autocorrelations, i.e., the memory effect, is a short-range angular dependent intensity correlation with a small angular width. Within the memory effect, the ballistic photons play a central role in the scattering imaging. It is widely accepted that only the ballistic light intensities can be used for the retrieval of the object information, and the scattered light distributions are regarded as noises. In this scheme, we can write the autocorrelation of the speckle pattern as

$$I \otimes I \approx \sum_{\Delta\varphi_n=0}^{\Phi} [(O \otimes O)C_n](\Delta\varphi_n) + \sum_{\Delta\varphi_n=\Phi}^{\pi} S_{\text{noise}}(\Delta\varphi_n), \quad (2.1)$$

where I indicates the measured intensity of speckle pattern, \otimes is an autocorrelation operation, and O denotes the intensity of the object. Φ is the angular width of the memory effect. Here we discretized the commonly used equation in the integral format [34] for the convenience of treating digital image and sampling. The discretization process and derivation of Eq. (2.1) is given in the Appendix. We adapt the polar coordinate system. $\Delta\varphi_n$ denotes the angle between the beams incident and transmitted through the scatterer. Or we can regard it as the angle between the n th pixel (n th circular ring around the optical axis) on the imaging plane and the optical axis with respect to the origin on the scatterer, when we exam the memory effect with the retrieved image and the field of view. The first part of Eq. (2.1) represents the object autocorrelation contributed by the memory effect, and the second term describes the noise. The correlation function C_n is a coefficient that describes the memory effect. Theoretical analysis indicates that it relates with the autocorrelation of the point spread function of the system (see the Appendix). The memory effect region lies in the existence area of the ballistic photons. That means the scattered photons have no contribution to the imaging. Generally, C_n is a sharp distribution and decreases with the increase in angle $\Delta\varphi_n$. That fact indicates

that, within the first term, there still exist noises contributed by the scattered photons. These noises degrade the image quickly at the edge. The theoretical estimation of the correlation C_n [32,42] is given by

$$C_{\text{theory}}(\Delta\varphi_n, L_{\text{eff}}) = [k\Delta\varphi_n L_{\text{eff}} / \sinh(k\Delta\varphi_n L_{\text{eff}})]^2, \quad (2.2)$$

where k is the wave number, and L_{eff} is the effective thickness of the scatterer. Theoretical estimation gives a FOV width of $\sim 3\lambda/(4\pi L_{\text{eff}})$ (half width at half maximum of C_{theory}). We can regard it as the theoretical maximum width of the memory effect. However, this theoretical prediction is extremely ideal, current experimental data usually suggest much narrower widths.

The first term in Eq. (2.1) only exists with the existence area of the ballistic photons. Usually the region that the ballistic photons exist are more wider than Φ . The contributions of the ballistic photons are mostly located at the center of $I \otimes I$. Few ballistic photons locate with a certain region outside but are immersed within the scattered photons, which are described by the second term, the noise term. From this perspective, we can recollect more ballistic photons from the second term and subdue noises and, therefore, expand the width of the memory effect for Φ to a broader one Φ' . We can rewrite Eq. (2.1) into

$$I \otimes I \approx \sum_{\Delta\varphi_n=0}^{\Phi'} [(O \otimes O)C_n](\Delta\varphi_n) + \sum_{\Delta\varphi_n=\Phi'}^{\pi} S_{\text{noise}}^{\text{scat}}(\Delta\varphi_n). \quad (2.3)$$

Our task is to tailor the coefficient C_n , making it more flatter and reasonably high and cleaning the noises both inside and outside the expanded memory effect region. The background noise parts are mostly of high spatial frequencies and can be eliminated grossly in the recording process of the speckle pattern, for example, with spatially low-pass filtering. We must tailor C_n in the computational reconstruction process.

The primary technique to select the ballistic photons and roughly reduce the background noise is the spatially low-pass filtering. Chen *et al.* employed a low-pass filter with an iris in the Fourier domain of a $4f$ system [38]. In our preliminary experiment, we also use a small aperture, just behind the scatterer, to choose the ballistic photons in the propagation process. The diameter of the aperture should surpass the width of the autocorrelation peak to ensure all the information of the object passes through. In this case, most of the scattered photons with high frequencies will be discarded. However, the performance of the small aperture to extend the memory effect region is limited because there still exist certain amounts of background noise with high frequencies. In addition, most of the noises in the signal term $\sum_{\Delta\varphi_n=0}^{\Phi'} [(O \otimes O)C_n](\Delta\varphi_n)$ are still untouched. In the following, we propose the autoshrinking algorithm to further expand the range of the memory effect, denoise, and improve the image quality.

The small aperture is physically real and can be regarded as a pretreatment in experiments, however, we can also employ an imaginary aperture in the retrieval process. The measured intensity of the speckle pattern is a superposition of the ballistic photons and the multiple scattered photons, i.e., the signal and the noises. The automatic shrinking algorithm can separate the ballistic beam intensity from the superposition

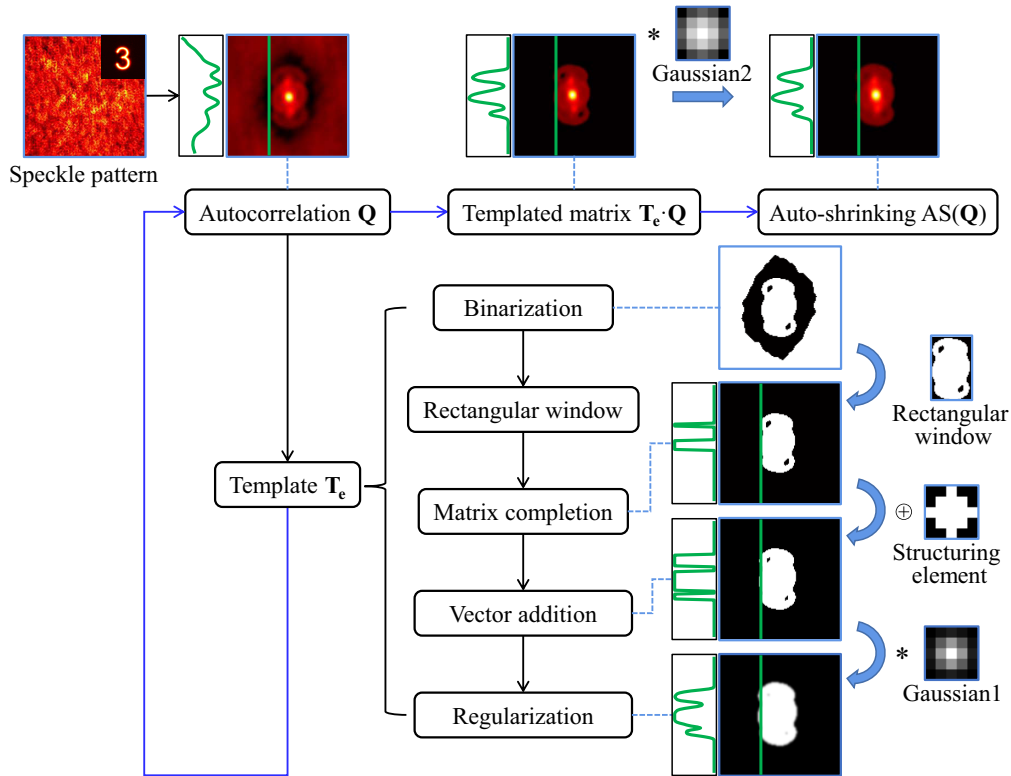


FIG. 1. Schematic of the autoshrinking algorithm. The algorithm includes modified filters and template calculation. The longitudinal profile of each process represented by a green curve, which indicates the photon distribution. The algorithm achieves a higher correlation coefficient of the memory effect $C_n \approx 1$ with the speckle pattern as the only available information.

image and eliminate noises caused by the scattered photons simultaneously. The algorithm is inspired by shrinking support used in the diffraction imaging [43]. The aim of the autoshrinking algorithm is to find an optimal autocorrelation function of speckle pattern with signal enhancement and denoising. Figure 1 shows the calculation processes of the autoshrinking algorithm. The subfigures in the upper row include the speckle pattern, the autocorrelation of the speckle pattern, template sampled autocorrelation function, and finally the optimal autocorrelation function after a Gaussian denoising. The lower columns represent the generation of the template \mathbf{T}_e , the imaginary aperture, and the regularization. We generate the template \mathbf{T}_e by adaptively shrinking the autocorrelation of speckle pattern \mathbf{Q} to its peak region with the following operations,

$$\mathbf{T}_e = \{\text{mc}[\text{bin}(\mathbf{Q})\mathbf{W}] \oplus \mathbf{B}\} * \mathbf{G}_1, \quad (2.4)$$

where \oplus and $*$ denote vector addition and convolution, respectively. Generally, around the “island” of the center peak of \mathbf{Q} , there exist the “sea” of noises, complicatedly tangled with ballistic photons and scattered photons in various different scattering regimes. The noises will immerse the edge part of correlation function which is also useful for recovering the object. Researchers regard this central peak as the memory effect region, therefore, in experiments, the width of the memory effect Φ is much narrower than the theoretical predicted one. The autoshrinking algorithm cleans the edge part of the correlation peak and utilize the ballistics photons in this area for imaging. In Eq. (2.4), we first employ the binarization to separate these two areas by setting the minimal level

of noise around the peak to zero and other areas to one. We then utilize a rectangular window \mathbf{W} , whose size is chosen according to the shape of the zero profile of $\text{bin}(\mathbf{Q})$, to select the peak of \mathbf{Q} and assign the pixels out of the window to zero through the matrix completion mc . In order to expand the area of scattering imaging, the width of the peak region should be increased. Thus, we utilize the vector addition with the structuring element \mathbf{B} to dilate the template. \mathbf{B} is a binary pixelwise solid circle with an adjustable radius, that can control the amount of dilation. Finally, in the regularization process, the dilated template convolves with the Gaussian kernel \mathbf{G}_1 to denoise in the outer part and prevent overfitting in the signal enhancement. The lower columns in Fig. 1 list these processing in detail. We also plot section profiles in green curves at the edge of the center peak to demonstrate the effects of extension and denoising.

In the generation of the template \mathbf{T}_e , we dilate the central peak to a broader one to include more ballistic photons and use the Gaussian low-pass filter \mathbf{G}_1 to suppress the noise. This will take effect when we use the template to choose the shrunk autocorrelation function. The final optimal autocorrelation function is given after another Gaussian low-pass filtering as

$$\text{AS}(\mathbf{Q}) = (\mathbf{T}_e \cdot \mathbf{Q}) * \mathbf{G}_2, \quad (2.5)$$

where \mathbf{G}_2 represents the second Gaussian filter. The performance of the autoshrinking algorithm is displayed in the upper right of Fig. 1, i.e., the optimal autocorrelation function $\text{AS}(\mathbf{Q})$. As we can immediately note the autoshrinking process directly discards the background noise. The Gaussian denoising and the regularization processes will reduce

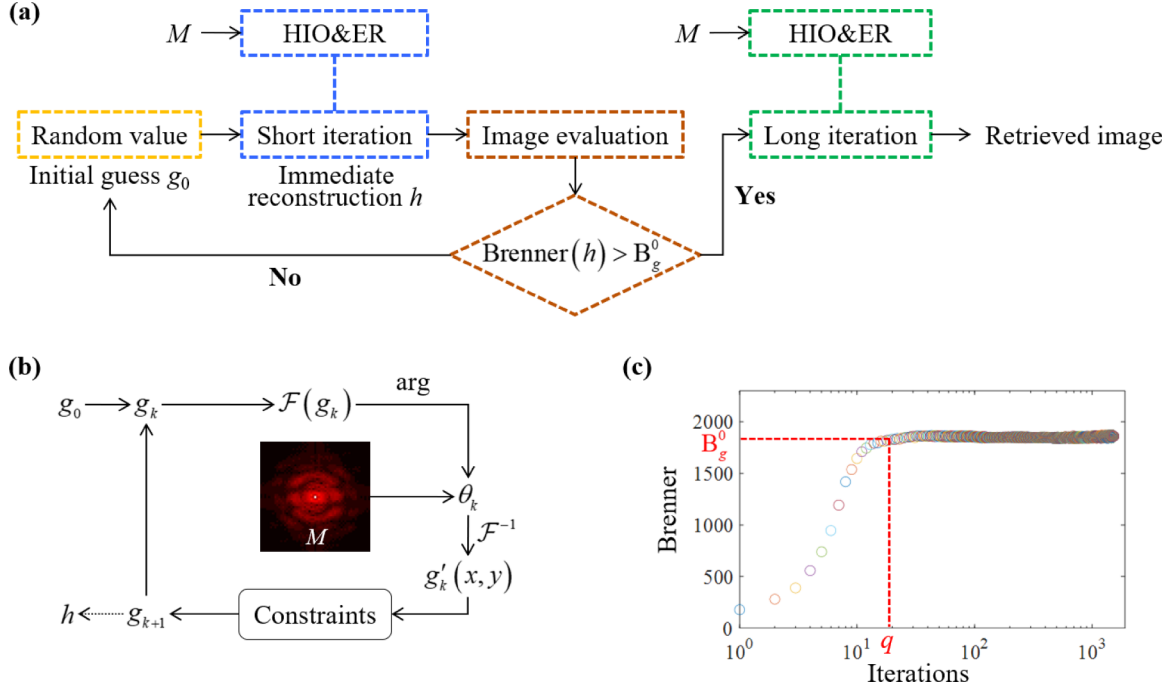


FIG. 2. Block diagram of the pretreatment iteration algorithm. The initial guess g_0 input to (a) the short iteration to produce an immediate reconstruction $h(x, y)$. (b) A brief diagram of the retrieval process with the HIO-ER algorithm. (c) An example of Brenner function. It serves as the constraint in the pretreatment iteration with the merit \mathbf{B}_g^0 . The reserved g_0 continues to a long iteration for a reconstruction. \mathcal{F} is the Fourier transform, and \mathcal{F}^{-1} is the inverse Fourier transform.

the noise and enhance coefficients of C_n within the entire expanded area effectively. These processes are nonlinear. They can broaden and flatten the memory effect region and, therefore, enlarge the effective imaging area.

We can choose a proper-sized \mathbf{B} so that the template \mathbf{T}_e includes the object scale l_0 . Therefore, the maximum width can be enhanced from Φ to $\Phi' \approx l_0/2l_1$ as

$$\text{AS}(\mathbf{Q}) \approx \sum_{\Delta\varphi_n=0}^{l_0/2l_1} (O \otimes O)(\Delta\varphi_n), \quad (2.6)$$

where l_1 is the distance between the object and the scatterer. The correlation coefficient $C_n \approx 1$. Different from the round hole used in the small aperture filter, the autoshrinking algorithm shrinks to the edge of a speckle autocorrelation peak by the memory effect. Therefore, the algorithm is valid for arbitrary-shaped objects.

For the final retrieval of the object image, its magnitude of the Fourier spectrum M can be approximately generated as

$$M = |\mathcal{F}\{O\}| \approx \sqrt{|\mathcal{F}\{\text{AS}(\mathbf{Q})\}|}, \quad (2.7)$$

where we use the Wiener-Khinchin theorem and \mathcal{F} denotes the Fourier transform. The missing Fourier phase is retrieved by a phase retrieval algorithm and accelerated by our pretreatment iteration algorithm.

We use the hybrid input-output and error reduction (HIO-ER) phase retrieval algorithms [30,34] for the reconstruction of the objects as shown in Fig. 2. Unlike the iteration processes in the previous studies [13,40,41], we concentrate more on an initialization pretreatment in order to quickly get an accurate retrieval with less iteration steps. The iterative type algorithm is usually sensitive to its initial value. Therefore, we

set an initial pretreatment testing iteration, called the “short iteration” process. We employ a gradient function as a no-reference perceptual quality assessment to select the initial value that can converge quickly. The flow chart in Fig. 2(a) actually depicts the entire process of generating the retrieved image. The loop shows the pretreatment iteration algorithm, which includes a short iteration and an evaluation. Once the immediate reconstruction satisfies a preset in the evaluation, the iteration will continue and complete the phase retrieval process. The detailed descriptions of the pretreatment iteration algorithm are given below.

In step 1, we select an initial random guess g_0 and run the phase retrieval algorithm, Fig. 2(a), for q iterations (~ 10 – 100) in the short iteration process. An immediate reconstruction $h(x, y)$ of the object is acquired. Here, the magnitude of the spatial Fourier spectrum M is required as the obtained amplitude. The quality of $h(x, y)$ decides to reserve or abandon this initial guess g_0 . The HIO-ER phase retrieval algorithm is briefly illustrated in Fig. 2(b). A real image g_k should obey the physical constraint that every pixel value should be non-negative and real.

In step 2, we employ a Brenner gradient function [44,45] to assess the immediate reconstruction $h(x, y)$,

$$\text{Brenner}(h) = \sum_{x=1}^M \sum_{y=1}^N [h(x, y) - h(x+2, y)]^2, \quad (2.8)$$

where M and N are the dimensions of an MN image $h(x, y)$. Statistically a clear and meaningful image will have a high gradient value than a blurred one. We depict an example curve of the Brenner function in Fig. 2(c).

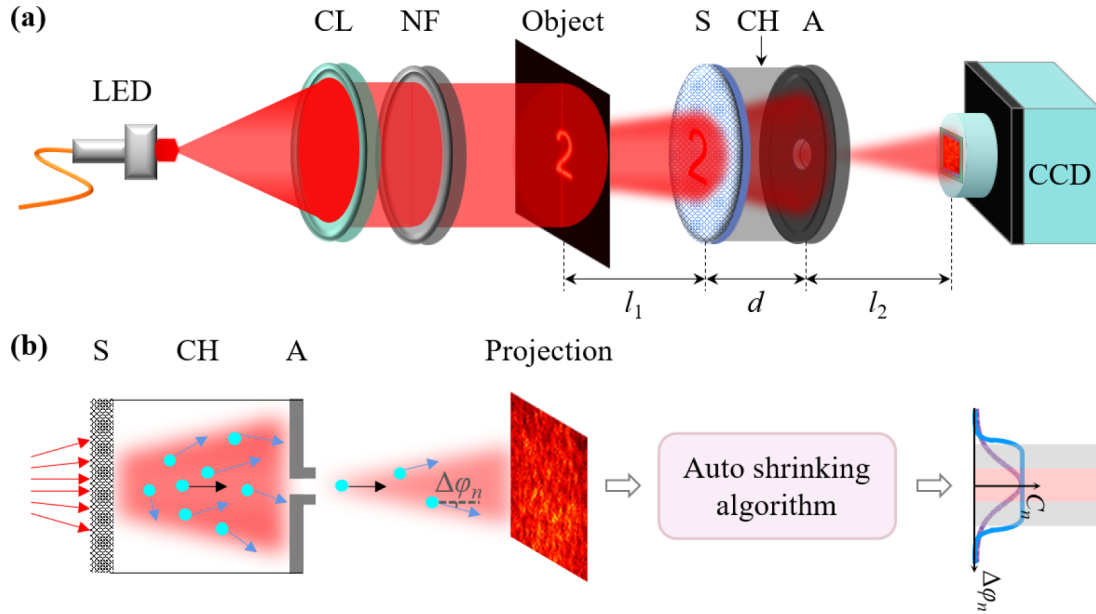


FIG. 3. Schematic of the apparatus for imaging through a scattering medium. (a) The optical setup for a single-shot scattering imaging. Light-emitting diode: LED; an incoherent source with central wavelength of 625 nm; collimated lens: CL; narrow-band filter: NF; cylindrical hood: CH; scatterer: S; small aperture: A; and the camera: CCD. (b) The conceptual schematic our proposal. The first part indicates the photons manipulation by the small aperture, the second part is the auto-shrinking calculation from the speckle pattern.

In step 3, we can set a merit \mathbf{B}_g^0 , as shown in Fig. 2(c), to examine the immediate image $h(x, y)$. If $\text{Brenner}(h) > \mathbf{B}_g^0$, then the immediate result is acceptable and the iteration can continue for several hundred steps in the long iteration process, by feeding $h(x, y)$ as g_0 in Fig. 2(a). Otherwise, the short iteration will stop and repeats by picking another initial guess g_0 .

The final output of the long iteration retrieves the object, with only hundreds of iterations, much shorter than the iterative processes in the previous works.

III. EXPERIMENTS AND DATA PROCESSING

We demonstrate the effectiveness of our technique in experiments and computational retrievals with the setting illustrated in Fig. 3. Figure 3(a) depicts the optical setup. A beam from a LED with the central wavelength of 625 nm (fiber-coupled LED, 625 nm, Thorlabs M625F2) is modulated by a collimated lens ($f = 20$ cm) and then passes through a narrow-band filter (632 ± 15 nm) to form a spatially incoherent narrow-band illumination. We use negative objects created by lithography as the targets. Four sets of objects are used in the experiments with sizes of 1.0, 2.0, 3.0, and 4.0 mm, respectively. The scattering medium is a 220 grits (220 grits, Thorlabs DG10-220-MD) 2-mm-thick ground glass with $L_{\text{eff}} = 61 \mu\text{m}$. A CCD camera (Point gray 2016 \times 2016 pixels, $3.1 \mu\text{m}$ of pixel size) is employed to capture the intensity of the speckle pattern. The object and the CCD camera are placed on two sides of the scatterer. The scatterer connects the small aperture with a cylindrical hood (CH). The distances among the object, the scatterer, the aperture, and the CCD camera are l_1 , d , and l_2 , respectively. By default, the experiments are performed with $l_1 = 50$, $d = 2.0$, and $l_2 = 10$ cm. The diameter of the aperture is adjustable

and should be greater than the size of the autocorrelation peak [30]. Figure 3(b) illustrates an abstract scheme that we select the ballistic photons by the aperture in experiments and enhance the coefficient C_n of the memory effect by the auto-shrinking algorithm in the computational imaging.

We capture the speckle patterns of the objects with four different sizes, under two imaging conditions of with and without the aperture. Each set of object has eight digits from 1 to 8 and several symbols. To demonstrate the robustness of our algorithms to possible random variations in the experiments, we take these speckle patterns in about 1 week. The experimental data are divided into three groups to characterize the effectiveness of our method from different perspectives.

Group 1 tests the ability to expand the memory effect region of the small aperture filter.

Group 2 tests the performance of the auto-shrinking algorithm in imaging exceeding the memory effect width by shrinking the speckle autocorrelation to its peak region. We take the second set of object (2.0-mm size with line width of $300 \mu\text{m}$) for the demonstrations. We choose a binary circle with a 5×5 size as the structuring matrix \mathbf{B} . The Gaussian filters \mathbf{G}_1 and \mathbf{G}_2 are 5×5 matrices with variances of $\sigma = 1.0$ and $\sigma = 2.0$, respectively. This group also examines a combination of the auto-shrinking algorithm and the small aperture. Then, the quick and accurate convergence of the pretreatment iteration algorithm are quantified. We calculate the success rate and rebuilding time of 700 reconstructions by the algorithm. The speckle pattern for each object is reconstructed 100 times. We then recover off-centered objects from the speckle patterns by modifying the auto-shrinking algorithm.

Group 3 tests the enhancement of memory effect with larger sized object (4.0-mm scale with a linewidth of $600 \mu\text{m}$). The FOV width of the retrieval images can exceed the maximum width predicted by theory.

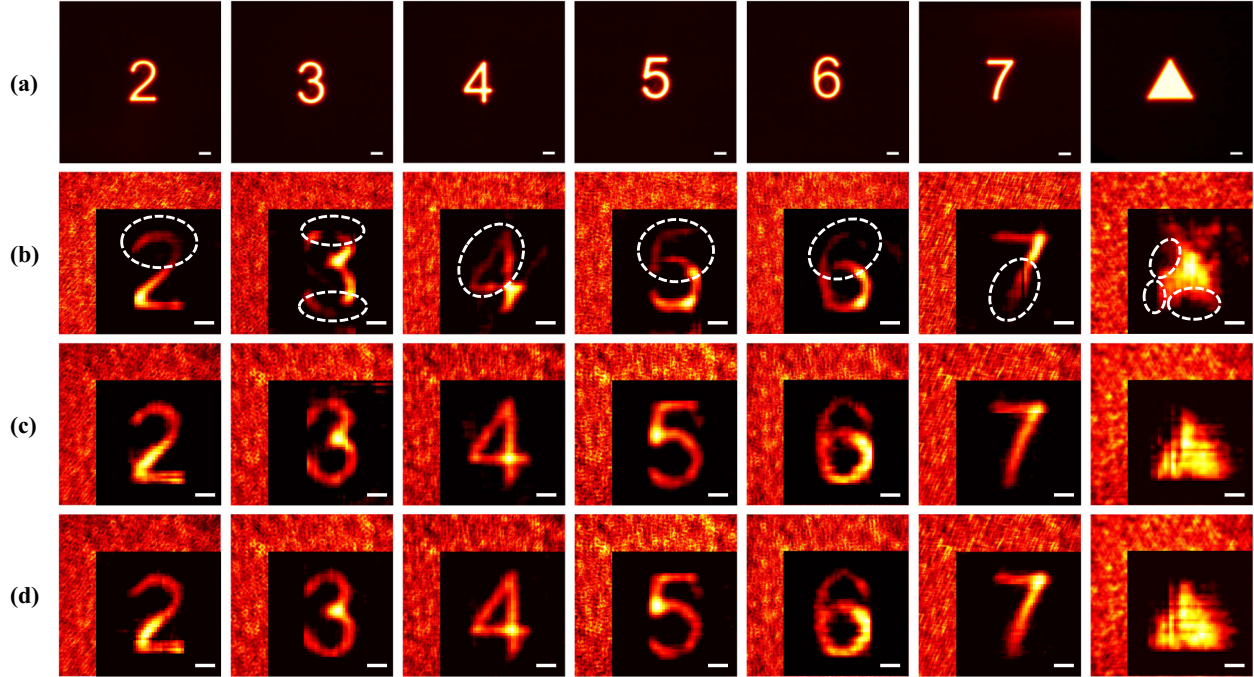


FIG. 4. The imaging performance with the small aperture. (a) The objects of six digit and a triangle symbol. (b) The images reconstructed from raw speckle patterns by the phase retrieval algorithm with 10200 iterations. The dashed circle indicates the nonimaging region for each object. (c) and (d) The reconstructions of the speckle patterns with the small aperture with 3825 iterations in common phase retrieval algorithm and with 102 and 663 iterations in the pretreatment algorithm, respectively. The scale bars indicate 0.5 mm at the object plane.

The number of the noise points on the measured image increases with the exposure time. In the long exposure (~ 1 s), we employ the downsampling technique to reduce the noise points. The speckle pattern downsampled from 2016×2016 to 512×512 pixels is used as the data for the calculation and testing of the proposed algorithms. The computational complexity is $O(N^2 \log N)$ for an $N \times N$ measurement area. For the cubic convolution interpolation, the white noise points in the experimental data significantly reduce after the downsampling and it may cause the loss of imaging details. However, this trade-off is demonstrated to be more instructive than disadvantageous.

IV. RESULTS AND DISCUSSIONS

In the first experiment, we examine the ability of expanding the FOV by the small aperture (Group 1) as shown in Fig. 4. Figure 4(a) displays the objects, six digits and a triangle symbol. Their corresponding speckle patterns and retrievals are presented in the backgrounds and the forefront images in Figs. 4(b)–(d), respectively. The retrievals in Figs. 4(b)–(d) represent the cases of without aperture, with aperture, with aperture, and pretreatment iteration, respectively. The white circles in Fig. 4(b) indicate the missing parts that are outside the memory effect region. However, these external regions outside the memory effect have been restored with the small aperture filtering [see Figs. 4(c) and 4(d)].

In the reconstructions, the common phase retrieval algorithm usually needs 10200 iterations to rebuild an object from the raw speckle pattern [Fig. 4(b)]. The reconstruction from the speckle pattern with aperture by the phase retrieval al-

gorithm still costs 3825 iterations [Fig. 4(c)]. However, in Fig. 4(d), the pretreatment iteration algorithm retrieves the object from the speckle pattern with aperture only with 102 and 663 iterations. That fact demonstrates that our algorithm can quickly find the optimal solution and converge with high success rate.

In the second experiment, we prove that the autoshrinking algorithm can enhance the correlation to broaden the high-fidelity imaging area of the memory effect (Group 2). First, we compare the similarities between the autocorrelations of the objects and their speckle autocorrelation functions with the autoshrinking algorithm as shown in Fig. 5. The comparisons directly reveal how the correlation coefficient C_n is enhanced. Figures 5(a) and 5(b) are the objects and their autocorrelations, respectively. Figures 5(c)–(e) are the autocorrelations of raw speckle patterns with the autoshrinking algorithm and with the autoshrinking algorithm and aperture, respectively. We calculate the mean-square errors (MSEs) of the selected areas of the speckle autocorrelations with the corresponding truth values [Fig. 5(b)] and display these MSEs on the bottoms of each subfigure. Obviously, the quality of the retrieve image is better with a higher C_n and a lower MSE. The white outlines indicate the calculation area according to the expanded central peak region in the autoshrinking process. The error of the raw speckle autocorrelation in Fig. 5(c) is almost two times greater than autocorrelation by the autoshrinking algorithm in Fig. 5(d) and that of the autoshrinking algorithm with the aperture in Fig. 5(e). Therefore, the object autocorrelation and the result of the autoshrinking algorithm [Figs. 5(b) and 5(e)] show an excellent resemblance to each other. Certainly, the lower error paves the way to enhance the recovery quality.

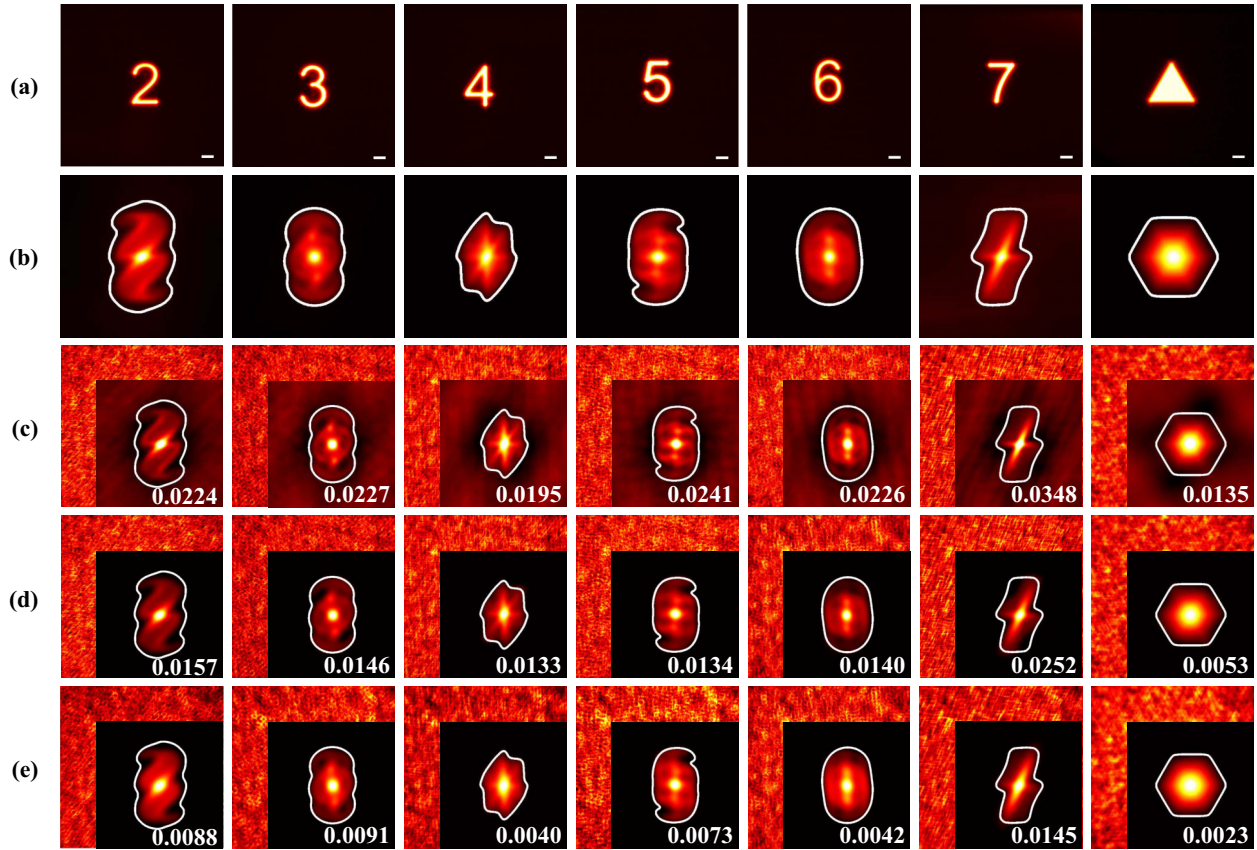


FIG. 5. Correlation enhancement by the autoshrinking algorithm. (a) Objects and their (b) autocorrelation patterns. (c) The autocorrelation of the raw speckle images. (d) and (e) are the results of the autoshrinking algorithm without and with the small aperture, respectively. All the autocorrelations are normalized. The MSEs of the selected areas are denoted at the bottom right. The scale bars correspond to 0.5 mm at the object plane.

Figure 6 shows the reconstructions with autoshrinking algorithm. Figure 6(a) is the objects. Figure 6(b) displays the recovery of the raw speckle pattern with a limited memory effect region. We then demonstrate the reconstructions with the autoshrinking algorithm without and with the small aperture in Figs. 6(c) and 6(d), respectively. The imaging results display an excellent resemblance to the object in exceeding the maximum angular width of the memory effect in experiments Φ . The region with the coefficient C_n higher than 0.98 is regarded as the high-fidelity area. There is no high-fidelity area in the raw speckle retrieval. After expanding the memory effect region, $\sim 78\%$ of the reconstruction by the autoshrinking algorithm fulfills that standard [Fig. 6(c)]. For the combination of the small aperture and the autoshrinking algorithm, there is an 80% area of the recovery that meets the high-fidelity standard as shown in Fig. 6(d). That may indicate that the roughly denoising operation by the small aperture can help autoshrinking to reduce more noises within the expanded region. All the Fourier phases of Fig. 6 are retrieved by our pretreatment iteration algorithm.

We quantify the performance of the pretreatment iteration algorithm in the retrieval processes with the large FOVs. In Table I, AS + PR (phase retrieval) and AS + PI (pretreatment iteration) denote the recovering success rate of the combination of the autoshrinking algorithm with and without the

pretreatment iteration, respectively. Time_{PR} and Time_{PI} are the running time of the phase retrieval and pretreatment iteration algorithms of the combinations. The success rates of the pretreatment iteration algorithm are ~ 2.0 times than that of the phase retrieval one. Even including all initialization processes, the running time of the pretreatment iteration can significantly drop to $\sim 1/3$ of the running time consumed by the common phase retrieval algorithm.

TABLE I. Success rates and running times of the phase retrieval algorithm and the pretreatment iteration algorithm. The data are obtained from the retrievals with large FOVs. The size of the target is 2.0 mm with a linewidth of 300 μm . All the time consumptions are for 100 reconstructions.

Target	AS + PR (%)	Time_{PR} (s)	AS + PI (%)	Time_{PI} (s)
2	28	238.91	72	85.73
3	26	262.21	45	62.80
4	22	230.35	52	56.59
5	34	247.55	69	64.72
6	27	224.66	47	45.55
7	44	236.58	74	52.68
Triangle	32	227.46	69	46.61

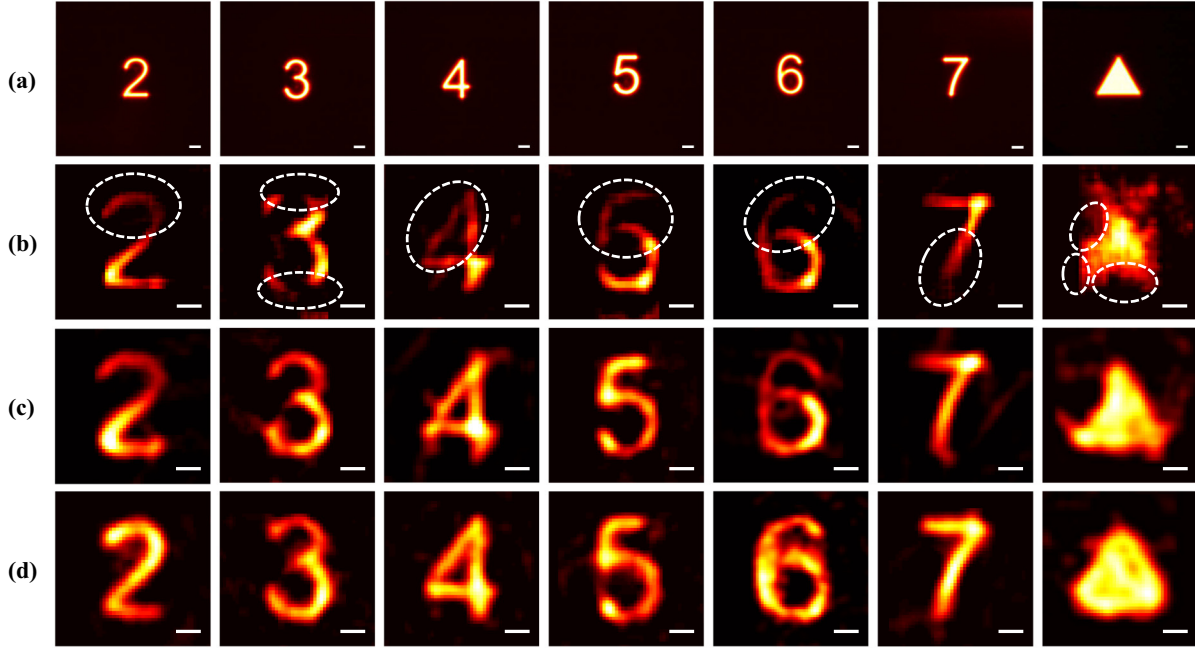


FIG. 6. The retrievals of high-fidelity images in larger FOV with autoshrinking algorithm. (a) The objects. (b) The reconstructions of the raw speckle patterns. (c) and (d) are the recovered images by the autoshrinking algorithm without and with the aperture, respectively. The Fourier phase of all images in (b)–(d) are retrieved by the pretreatment iteration algorithm. The scale bars denote 0.5 mm at the object plane.

We also test the ability of our autoshrinking algorithm to recover off-centered objects with a broader view as shown in Fig. 7. The relative shift between the object and the center is 2.0 mm in the horizontal direction. The measurements here include the speckle pattern of the central object I_0 and the speckle of the off-center object I_{off} . In the modified algorithm, we use the cross-correlation of I_{off} and I_0 instead of the autocorrelation. Figures 7(a) and 7(b) are the off-centered

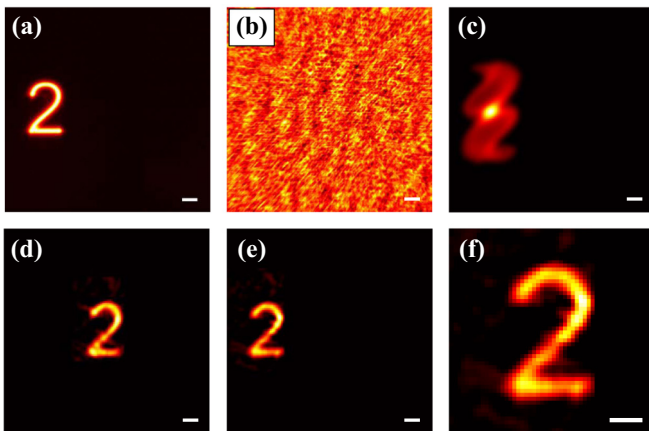


FIG. 7. Imaging an off-centered object through the scatterer by the modified autoshrinking algorithm. (a) The digit 2 with a 2.0-mm relative shift from the center and its (b) speckle intensity pattern. (c) The autoshrunked cross-correlation function. (d) Object recovered from autocorrelation, the location of object is undefined but it can be restrained to the center. (e) The recovered object from the cross-correlation by the modified algorithm. (f) Zoomed image of (e). The scale bars correspond to 0.5 mm at the object plane.

object and its speckle pattern. The autoshrunked optimal cross-correlation of two speckle patterns is shown in Fig. 7(c). We can still use the autocorrelation of the off-centered speckle pattern, however, its position information will be undefined. Figure 7(d) is the retrieval image with the autocorrelation. The retrieved image is restrained at the center. The modified autoshrinking algorithm can reconstruct the object right in its coordinate [Fig. 7(e)] with high quality [see the zoomed image in Fig. 7(f)].

We calculate the coefficient of the angular correlation C_n from the experimental data and compare our scheme with other techniques. In the quantification of C_n , we use expression $I(\Delta\varphi_n) \otimes I(\Delta\varphi_n) = [(O \otimes O)C_n](\Delta\varphi_n)$ and adapt the zero-mean normalized cross-correlation [46] as

$$C_{\text{exp}} = \frac{\sum_x [r(x, y) - \bar{r}][t(x, y) - \bar{t}]}{\sqrt{\sum_x [r(x, y) - \bar{r}]^2} \sqrt{\sum_x [t(x, y) - \bar{t}]^2}}, \quad (4.1)$$

where we turn the coordinates to the Cartesian system with the origin at the center and $r(x, y)$ and $t(x, y)$ denote the element of the MN intensities for the reference and target, \bar{r} and \bar{t} denote their corresponding mean intensities along the x direction for each y , respectively. The sampling step in y direction is 4 pixels, about 0.05 mrad. The reference and the target, r and t , represent the autocorrelation of the object [see Fig. 5(b)] and the autocorrelation of its speckle pattern, respectively. We compare C_n (C_{exp}) with various methods include, theoretical calculation, raw, aperture, autoshrinking, aperture, and autoshrinking, multimode fiber illumination (MMF) [37] and low-pass Fourier domain filtering (LPF) [38]. The results are shown in Fig. 8.

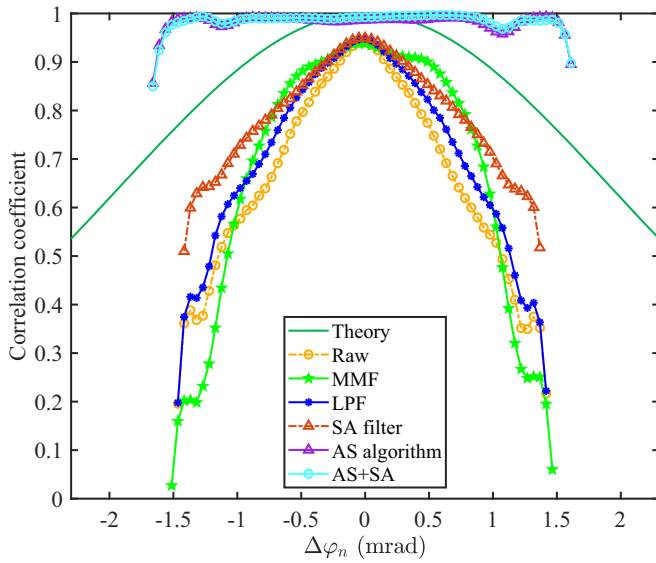


FIG. 8. Calculations and comparisons of the correlation coefficients C_{exp} for different methods with the theoretical prediction C_{theory} . The dark-green solid curve indicates C_{theory} . All the calculations are based on normalized autocorrelation distributions. The object is the digit 2 with size of 2.0 mm. SA: small aperture; AS: autoshrinking.

Theoretical estimation indicates that the region with coefficient C_n greater than 0.6 can be used for imaging. In this case the theoretical prediction (solid dark-green curve) seems extremely different from the practical one. The imaging width of the raw retrieval (orange circle-dashed curve) is only ~ 0.8 mrad (half-width), which is the lowest among those methods. The C_{exp} with the MMF (green star-line curve) and the LPF (blue asterisk-line curve) are larger than that of raw, but the expanding is limited. The method with small aperture (red triangle-dashed curve) is better than those three. The best techniques for expanding the imaging area are the schemes with autoshrinking and with autoshrinking and aperture (the purple triangle-line curve and the cyan circle-line curve). They are nearly the same because the autoshrinking algorithm dominates this process. The FOV widths in these two schemes

can be enhanced to ~ 1.7 mrad. The correlation coefficient $C_{\text{exp}} \approx 1$ within this region, that means the autoshrinking algorithm can retrieve high-fidelity images.

The corresponding data of C_{exp} with different approaches are displayed in Table II. C_{theory} lists here only for a reference. We compare the imaging ($C_{\text{exp}} > 0.6$) and high-fidelity imaging ($C_{\text{exp}} > 0.98$) areas for those methods.

Our strategy of extending the memory effect is according to the size of object. The aim is clear that we intend to get the image of the entire object with high fidelity. Therefore, the theoretical estimation of maximum width Φ' is currently unavailable in our scheme. We can only expect the FOV in experiments approaching $\Phi' \approx l_0/2l_1$ by setting the size of \mathbf{B} . For the object with the size of 2.0 mm, the maximum FOV width is $\Phi' \approx 2.0$ mrad. The measurement indicates that the FOV can be $\Phi' \sim 1.7$ mrad. These two values are close and two times wider than that of raw retrieval. To further demonstrate the expanding power of the autoshrinking algorithm, we reconstruct the images from the experimental data (Group 3) for the object with the size of 4.0 mm. The retrievals are displayed in Fig. 9.

For the scattering imaging of an object with larger size, its speckle pattern has a wider distribution of the ballistic photons, and its autocorrelation peak should also be wider. Therefore, we add the amount of dilation in preparing the template \mathbf{T}_e with a larger structuring element \mathbf{B} (12×12 binary solid circle). The corresponding central peak area dilates from ~ 1.50 to ~ 1.64 mm. Figures 9(a)–9(d) display the objects, their speckle patterns, the raw retrievals, and the retrievals with the autoshrinking algorithm, respectively. From Fig. 9(d), we can see that the objects in their full size can be recovered with high fidelities. On the contrary, we cannot recognize the objects from the raw retrievals in Fig. 9(c) because a width of FOV ~ 0.8 mrad is too small to unveil the entire object.

We also qualify the correlation coefficient C_{exp} in this case and show the curves in Fig. 10. We only compare our autoshrinking technique with theoretical prediction and the experimental data of the raw retrievals. From the experimental data, we have $\Phi' \sim 3.0$ mrad for the autoshrinking algorithm, which surpasses the maximum half-widths of FOV by theory ~ 2.4 mrad and the raw retrievals by ~ 0.8 mrad.

TABLE II. The comparison of the expanding the FOV with different methods. The coefficient C_{theory} or C_{exp} larger than 0.6 can be used for imaging. The coefficient larger than 0.98 can achieve high-fidelity imaging. C_{theory} or $C_{\text{exp}} > 0.6$ and C_{theory} or $C_{\text{exp}} > 0.98$ are the maximum angles of the two regions. $\text{Average}_{0.6}$ and $\text{Average}_{0.98}$ are the average values of these regions.

Test	C_{theory} or $C_{\text{exp}} > 0.6$ (mrad)	$\text{Average}_{0.6}$	C_{theory} or $C_{\text{exp}} > 0.98$ (mrad)	$\text{Average}_{0.98}$
Theory ^a	4.13	0.85	0.79	0.99
Raw ^b	1.66	0.80		
MMF ^c	1.95	0.85		
LPF ^d	2.05	0.80		
SA filter (this paper)	2.64	0.80		
AS algorithm (this paper)	3.42	0.97	2.78	0.99
AS+SA (this paper)	3.37	0.98	2.88	0.99

^aReferences [32,42].

^bReference [30].

^cReference [37].

^dReference [38].

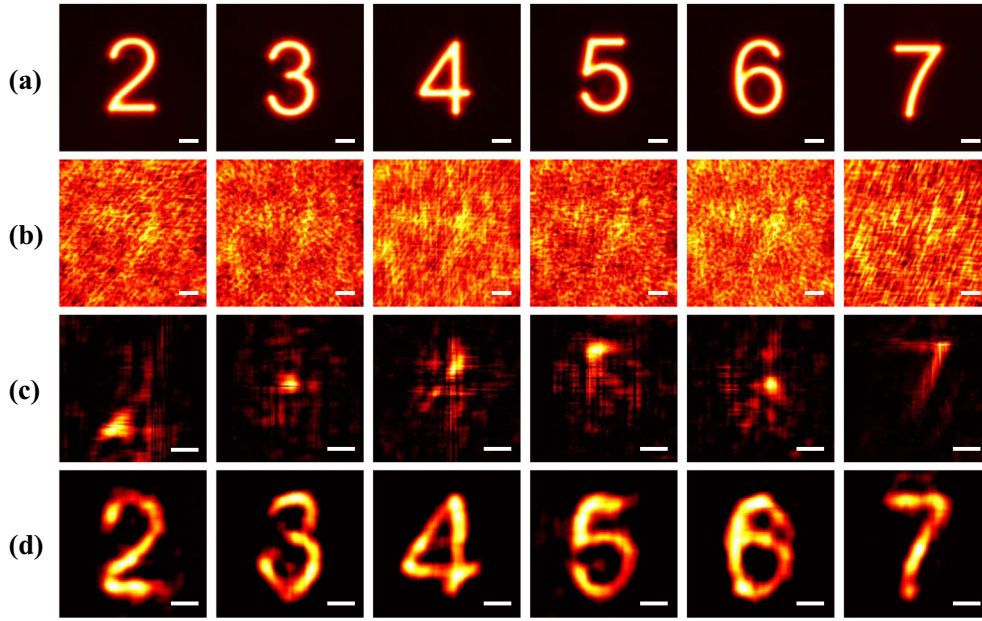


FIG. 9. Retrievals of objects with the size of 4.0 mm with autocorrelation algorithm. (a) The objects and (b) their corresponding speckle distributions. (c) The raw retrievals and (d) the retrievals with autoshrinking algorithm. The scale bars correspond to 1.0 mm at the object plane.

The autoshrinking algorithm is the core of this paper, that can break the limit of theoretical estimation of the maximum width of the memory effect. We assume that there should exist a boundary of our scheme in extending the memory effect because that effect is mostly of the property of the scattering imaging system and depends strongly on the characteristics of the scattering medium. Our method only chooses a certain region of the central correlation peak of the speckle pattern and enhances the ratio of the ballistic photons to the scattered

photons. We cannot rigorously preserve the ballistic photons and completely eliminate the scattered ones within this central peak region for there exist extremely complicated noise distributions. The power of the autoshrinking algorithm may demand more delicate denoising techniques. Nevertheless, our proposal demonstrate that it is effective to expand the width of the memory effect by manipulating the distribution of the photons at the central region of the autocorrelation function.

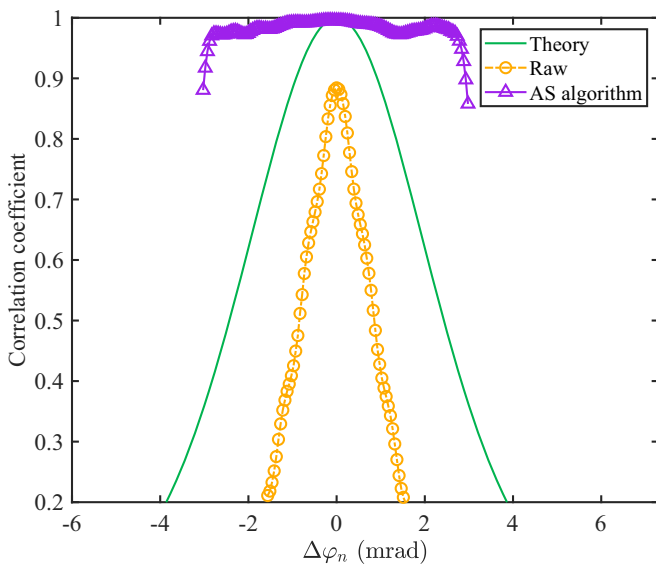


FIG. 10. Comparisons of the correlation coefficients C_{exp} of the autoshrinking scheme with theoretical prediction C_{theory} and the raw retrievals. The autoshrinking technique has wider FOV width than the theoretical prediction and the raw retrievals.

V. CONCLUSION

We have proposed and experimentally demonstrated the autoshrinking and the pretreatment iteration algorithms to significantly broaden the FOV of the speckle correlation scattering imaging with high-fidelity retrievals and high success rates. The autoshrinking algorithm can collect more ballistic photons by adaptively shrinking the speckle autocorrelation to the expanded central region and simultaneously eliminate the noises contributed by the scattered photons. The essence of the autoshrinking algorithm is to preserve the information of the object, as much as possible by enhancing the ratio of the ballistic photons to the scattered photons within the central area of the speckle autocorrelation. The width of the memory effect or the FOV can be enhanced by the autoshrinking algorithm, up to the width that can include the entire object with high-fidelity imaging. The correlation coefficient C_n of the expanded area can approach one. In the retrieval process, we set an additional constrain of the pretreatment, the Brenner gradient function, in the phase retrieval algorithm for selecting the optimal initial guess. The speed of the retrieval process and the success rate of reconstruction are enhanced. The experimental and the retrieval data confirm the effectiveness of our proposals. This prior-free and noninvasive imaging

technique may find broad applications in biomedical detections, communications, and industries.

CONFLICT OF INTEREST

The authors declare no conflicts of interest.

ACKNOWLEDGMENTS

This work was supported by National Natural Science Foundation of China (Grants No. 11874132, No. 61975044, and No. 12074094), and Interdisciplinary Research Foundation of HIT (Grant No. IR2021237).

APPENDIX: THE DISCRETIZATION ANALYSIS OF THE SPECKLE INTENSITY CORRELATION

In this Appendix we provide the discretization of the speckle correlation, which usually is represented in an integral form [34]. The discretization is straightforward, only substituting the integral with summation for the reason that we treat

the MN digital image. From this perspective, the discretized representation may be more convenient.

We adapt the polar coordinates. $\Delta\varphi_n$ is an angle between the n th pixel (the n th circular ring) on the imaging plane and the optical axis with respect to the origin on the scatterer plane. The intensity of the scattered beam I at angle $\Delta\varphi_n$ is the convolution of the object intensity O and the point spread function (PSF) of the system $\text{PSF}(\Delta\varphi_n)$ at the same angle. Thus, that can be expressed as

$$I(\Delta\varphi_n) = \text{PSF}(\Delta\varphi_n) * O(\Delta\varphi_n), \quad (\text{A1})$$

where $*$ is the convolution operation. The phase and intensity of the beam are different even with the same spreading direction due to the random nature of the scattered beam. The measured speckle displayed in Fig. 4 cannot directly resemble the original object behind the scatterer. To separate the object intensity from the speckle pattern, we employ the autocorrelation generated by the captured pattern,

$$\begin{aligned} I(\Delta\varphi_n) \otimes I(\Delta\varphi_n) &= [O * \text{PSF}](\Delta\varphi_n) \otimes [O * \text{PSF}](\Delta\varphi_n) \\ &= [O \otimes O](\Delta\varphi_n) * [\text{PSF} \otimes \text{PSF}](\Delta\varphi_n). \end{aligned} \quad (\text{A2})$$

The term $\text{PSF}(\Delta\varphi_n) \otimes \text{PSF}(\Delta\varphi_n)$ is also a sharp peak distribution and described as $C_n\delta$ [34]. Therefore, Eq. (A2) can be written as

$$I(\Delta\varphi_n) \otimes I(\Delta\varphi_n) = \begin{cases} [(O \otimes O) * \delta]C_n(\Delta\varphi_n), & \text{if } \Delta\varphi_n \in [0, \Phi], \\ S_{\text{noise}}(\Delta\varphi_n), & \text{if } \Delta\varphi_n \in (\Phi, \pi], \end{cases} \quad (\text{A3})$$

where δ is the Kronecker function that describes the existence of ballistic photons. For the ballistic photons $\delta = 1$, otherwise, for scattered photons $\delta = 0$. According to the unity of the memory effect and the spatial shift invariance [33], the optical memory effect is contributed by the ballistic photons. Generally, the width of the ballistic photons distribution is wider than that of the memory effect. Therefore, Eq. (A3) can be expressed as

$$I(\Delta\varphi_n) \otimes I(\Delta\varphi_n) = \begin{cases} [(O \otimes O)C_n](\Delta\varphi_n), & \text{if } \Delta\varphi_n \in [0, \Phi], \\ S_{\text{noise}}(\Delta\varphi_n), & \text{if } \Delta\varphi_n \in (\Phi, \pi]. \end{cases} \quad (\text{A4})$$

Here, we consider both forward scattering and backscattering. The maximum angle produced by a scattered beam is defined as π . Therefore, the autocorrelation of the total measured speckle pattern is written as Eq. (2.1) by summing Eq. (A4) with $\Delta\varphi_n$ from 0 to π .

-
- [1] A. M. Kingston, W. K. Fullagar, G. R. Myers, D. Adams, D. Pelliccia, and D. M. Paganin, Inherent dose-reduction potential of classical ghost imaging, *Phys. Rev. A* **103**, 033503 (2021).
- [2] A. P. Mosk, A. Lagendijk, A. Lagendijk, G. Leroose, and M. Fink, Controlling waves in space and time for imaging and focusing in complex media, *Nat. Photonics* **6**, 283 (2012).
- [3] M. Ren, J. Chen, D. Chen, and S.-C. Chen, Aberration-free 3D imaging via DMD-based two-photon microscopy and sensorless adaptive optics, *Opt. Lett.* **45**, 2656 (2020).
- [4] X. Nie, F. Yang, X. Liu, X. Zhao, R. Nessler, T. Peng, M. S. Zubairy, and M. O. Scully, Noise-robust computational ghost imaging with pink noise speckle patterns, *Phys. Rev. A* **104**, 013513 (2021).
- [5] D. Marima, B. Hadad, S. Froim, A. Eyal, and A. Bahabad, Visual data detection through side-scattering in a multimode optical fiber, *Opt. Lett.* **45**, 6724 (2020).
- [6] I. Gianani, A. Suprano, T. Giordani, N. Spagnolo, F. Sciarrino, D. Gorpas, V. Ntziachristos, K. Pinker, N. Biton, J. Kupferman, and S. Arnon, Transmission of vector vortex beams in dispersive media, *Adv. Photonics* **2**, 036003 (2020).
- [7] R. Horstmeyer, H. Ruan, and C. Yang, Guidestar-assisted wavefront-shaping methods for focusing light into biological tissue, *Nat. Photonics* **9**, 563 (2015).
- [8] G. Satat, M. Tancik, and R. Raskar, Towards photography through realistic fog, in *2018 IEEE International Conference on Computational Photography (ICCP)*, p. 1.
- [9] Y. Altmann, S. McLaughlin, M. J. Padgett, V. K. Goyal, A. O. Hero, and D. Faccio, Quantum-inspired computational imaging, *Science* **361**, eaat2298 (2018).
- [10] D. B. Lindell and G. Wetzstein, Three-dimensional imaging through scattering media based on confocal diffuse tomography, *Nat. Commun.* **11**, 4517 (2020).
- [11] R. Tobin, A. Halimi, A. McCarthy, M. Laurenzis, F. Christnacher, and G. S. Buller, Three-dimensional single-photon imaging through obscurants, *Opt. Express* **27**, 4590 (2019).

- [12] E. Edrei, and G. Scarcelli, Optical imaging through dynamic turbid media using the Fourier-domain shower-curtain effect, *Optica* **3**, 71 (2016).
- [13] M. Hofer, C. Soeller, S. Brasselet, and J. Bertolotti, Wide field fluorescence epi-microscopy behind a scattering medium enabled by speckle correlations, *Opt. Express* **26**, 9866 (2018).
- [14] X. Xie, Q. He, Y. Liu, H. Liang, and J. Zhou, Non-invasive optical imaging using the extension of the Fourier-domain shower-curtain effect, *Opt. Lett.* **46**, 98 (2021).
- [15] Z. Yan, C. Hu, Z. Li, Z. Li, H. Zheng, and X. Jin, Underwater photon-inter-correlation optical communication, *Photonics Res.* **9**, 2360 (2021).
- [16] F. Liu, Y. Wei, P. Han, K. Yang, L. Bai, and X. Shao, Polarization-based exploration for clear underwater vision in natural illumination, *Opt. Express* **27**, 3629 (2019).
- [17] Z. Wang, H. Liu, N. Huang, Y. Zhang, and J. Chi, Nonlinear reconstruction of weak optical diffused images under turbid water, *Opt. Lett.* **44**, 3502 (2019).
- [18] Z. Hosseinaee, M. Le, K. Bell, and P. H. Reza, Towards non-contact photoacoustic imaging [review], *Photoacoustics* **20**, 100207 (2020).
- [19] S. Rotter and S. Gigan, Light fields in complex media: mesoscopic scattering meets wave control, *Rev. Mod. Phys.* **89**, 015005 (2017).
- [20] K. A. Kondrat'ev, V. V. Marinyuk, D. B. Rogozkin, and S. V. Sheberstov, Enhancement of mesoscopic fluctuations in transmission of light through a disordered medium at grazing angles, *Phys. Rev. A* **103**, 013715 (2021).
- [21] Y. Kang, Y. Huang, and A. Z. Genack, Dynamics of transmission in disordered topological insulators, *Phys. Rev. A* **103**, 033507 (2021).
- [22] H. Jin, B. Hwang, S. Lee, and J.-H. Park, Limiting the incident NA for efficient wavefront shaping through thin anisotropic scattering media, *Optica* **8**, 428 (2021).
- [23] S. K. Sahoo, D. Tang, and C. Dang, Single-shot multispectral imaging with a monochromatic camera, *Optica* **4**, 1209 (2017).
- [24] L. Li, Q. Li, S. Sun, H.-Z. Lin, W.-T. Liu, and P.-X. Chen, Imaging through scattering layers exceeding memory effect range with spatial-correlation-achieved point-spread-function, *Opt. Lett.* **43**, 1670 (2018).
- [25] X. Xu, X. Xie, H. He, H. Zhuang, J. Zhou, A. Thendiyammal, and A. P. Mosk, Imaging objects through scattering layers and around corners by retrieval of the scattered point spread function, *Opt. Express* **25**, 32829 (2017).
- [26] Jeremy Boger-Lombard, and O. Katz, Passive optical time-of-flight for non line-of-sight localization, *Nat. Commun.* **10**, 3343 (2019).
- [27] E. G. van Putten, D. Akbulut, J. Bertolotti, W. L. Vos, A. Lagendijk, and A. P. Mosk, Scattering Lens Resolves Sub-100 nm Structures with Visible Light, *Phys. Rev. Lett.* **106**, 193905 (2011).
- [28] N. Bender, M. Sun, H. Yilmaz, J. Bewersdorf, and H. Ca, Circumventing the optical diffraction limit with customized speckles, *Optica* **8**, 122 (2021).
- [29] Z. Li, X. Nie, F. Yang, X. Liu, D. Liu, X. Dong, X. Zhao, T. Peng, M. S. Zubairy, and M. O. Scully, Sub-Rayleigh second-order correlation imaging using spatially distributive colored noise speckle patterns, *Opt. Express* **29**, 19621 (2021).
- [30] O. Katz, P. Heidmann, M. Fink, and S. Gigan, Non-invasive single-shot imaging through scattering layers and around corners via speckle correlations, *Nat. Photonics* **8**, 784 (2014).
- [31] S. Feng, C. Kane, P. A. Lee, and A. D. Stone, Correlations and Fluctuations of Coherent Wave Transmission through Disordered Media, *Phys. Rev. Lett.* **61**, 834 (1988).
- [32] I. Freund, M. Rosenbluh, and S. Feng, Memory Effects in Propagation of Optical Waves through Disordered Media, *Phys. Rev. Lett.* **61**, 2328 (1988).
- [33] H. Liu, Z. Liu, M. Chen, S. Han, and L. V. Wang, Physical picture of the optical memory effect, *Photonics Res.* **7**, 1323 (2019).
- [34] J. Bertolotti, E. G. van Putten, C. Blum, A. Lagendijk, W. L. Vos, and A. P. Mosk, Non-invasive imaging through opaque scattering layers, *Nature (London)* **491**, 232 (2012).
- [35] T. Wu, O. Katz, X. Shao, and S. Gigan, Single-shot diffraction-limited imaging through scattering layers via bispectrum analysis, *Opt. Lett.* **41**, 5003 (2016).
- [36] X. Li, J. A. Greenberg, and M. E. Gehm, Single-shot multispectral imaging through a thin scatterer, *Optica* **6**, 864 (2019).
- [37] R. Ma, Z. Wang, H. Zhang, W. Zhang, and Y. Rao, Imaging through opacity using a near-infrared low-spatial-coherence fiber light source, *Opt. Lett.* **45**, 3816 (2020).
- [38] M. Chen, H. Liu, Z. Liu, P. Lai, and S. Han, Expansion of the FOV in speckle autocorrelation imaging by spatial filtering, *Opt. Lett.* **44**, 5997 (2019).
- [39] X. Wang, X. Jin, and J. Li, Blind position detection for large field-of-view scattering imaging, *Photonics Res.* **8**, 920 (2020).
- [40] X. Wang, X. Jin, J. Li, X. Lian, X. Ji, and Q. Dai, Prior-information-free single-shot scattering imaging beyond the memory effect, *Opt. Lett.* **44**, 1423 (2019).
- [41] H. Yilmaz, E. G. van Putten, J. Bertolotti, A. Lagendijk, and W. L. Vos, Speckle correlation resolution enhancement of wide-field fluorescence imaging, *Optica* **2**, 424 (2015).
- [42] S. Schott, J. Bertolotti, J.-F. Leger, L. Bourdieu, and S. Gigan, Characterization of the angular memory effect of scattered light in biological tissues, *Opt. Express* **23**, 13505 (2015).
- [43] S. Marchesini, H. He, H. N. Chapman, S. P. Hau-Riege, A. Noy, M. R. Howells, U. Weierstall, and J. C. H. Spence, X-ray image reconstruction from a diffraction pattern alone, *Phys. Rev. B* **68**, 140101(R) (2003).
- [44] J. F. Brenner, B. S. Dew, J. B. Horton, T. King, P. W. Neurath, and W. D. Selles, An automated microscope for cytologic research a preliminary evaluation, *J. Histochem. Cytochem.* **24**, 100 (1976).
- [45] O. A. Osibote, R. Dengere, S. Krishnan, and T. S. Douglas, Automated focusing in bright-field microscopy for tuberculosis detection, *J. Microsc.* **240**, 155 (2010).
- [46] Y. Pang, B. K. Chen, S. Yu, and S. N. Lingamanaik, Enhanced laser speckle optical sensor for in situ strain sensing and structural health monitoring, *Opt. Lett.* **45**, 2331 (2020).